Human Computational Fluid Dynamics: From the Nose Model to the Real Nose*

Wolfgang Schröder

Institute of Aerodynamics, RWTH Aachen University
Wüllnerstraße 5 A, D-52062 Aachen

The following article summaries the work that has been performed at the Institute of Aerodynamics since roughly 2005 in the field of biomedical flows, a fantastic area where medicine, biology, and fluid mechanics interact. The focus of the discussion is on nasal cavity flows. It represents an excerpt of the work that has been jointly performed with I. Hörschler, M. Meinke, and A. Lintermann.

I. Introduction

The human nasal cavity must satisfy a variety of functions. Besides respiration it is responsible for moistening, tempering, and cleaning the air. These functions are expected to strongly depend on the complex internal geometry of the nasal cavity. Impaired nasal respiration especially under normal breathing conditions, i.e., in everyday life situations, is a common and widespread disease, which makes nose surgery one of the most often performed operations in the western world. Unfortunately, the success rate, i.e., the number of people having no problems after surgery, is by no means satisfactory. To enhance this situation, it is desired to numerically predict the flow field inside the nose and its relation to geometric changes. This can finally lead to a computer assisted surgery (CAS) tool, that will help on the one hand, to understand the flow in the extremely complex human nasal cavity and on the other hand, to derive criteria how to better predict the outcome and to improve the success of nose operations. This study contains some first steps to reach the long term goal of a rhino-CAS tool.

Before geometric changes of the nasal cavity can be analyzed from a fluid mechanical point of view, two fundamental questions have to be answered. First, in the literature the flow through the human nasal cavity is considered quasi steady due to a very low Strouhal number at normal breathing conditions. However, this assumption has never been thoroughly verified. The question arises whether or not this assumption holds independently from the mass flux or, in other words, from the Reynolds number. Therefore, in section III it will be clarified in which

* Der Vortrag wurde am 26.04.2013 anlässlich der Verleihung der Gauß-Medaille durch die Braunschweigische Wissenschaftliche Gesellschaft gehalten.

Reynolds number range the flow behaves quasi-steady to show when numerically less expensive steady state flow simulations can be performed. Furthermore, the unsteady nasal cavity flow field gives insight in the interesting phase of transition between inspiration and expiration. Second, the findings in the literature give a very unclear picture of the state of the nasal cavity flow. Many research groups consider the flow to be turbulent. Turbulence models are applied that are often invalid for this kind of internal flow. This turbulence assumption is primarily justified by the value of the Reynolds number based on the bulk velocity and the hydraulic diameter which is too rough an indicator for such an intricate internal flow. A comparison with a critical Reynolds number of Re = 2300 that indicates the change from laminar to turbulent flow at a pipe with circular cross section can at least be called questionable. Section IV evidences via numerical and experimental findings the flow at normal respiration to be well described by highly resolved laminar simulations.

The aforementioned issues will be addressed in the context of a model geometry of the human nasal cavity. In the next step, in Section V in which the influence of the geometric variation of the nasal cavity will be discussed no more model configurations but real nose geometries will be analyzed and the results with respect to velocity profiles, wall-shear, and heat transfer distributions will be juxtaposed for three human nasal cavities.

In brief, this article possesses the following structure. In the subsequent section, the numerical methods are only sketched. The steady-unsteady and laminar-turbulent issues are discussed in sections III and IV. The impact of geometric variations is analyzed in section V, before some conclusions are drawn in section VI.

II. Numerical Methods

The analyses of the model configurations are performed by a structured finite-volume method to approximately solve the Navier-Stokes equations of a three-dimensional fluid [1]. An explicit five-stage Runge-Kutta method of second-order accuracy is used for temporal integration. The spatial approximation is also of second-order accuracy using an advective upstream splitting method (AUSM) for the inviscid terms and centered discretizations for the remaining differentials. A more detailed description of the solver including the reference values for the non-dimensional Navier–Stokes equations is given in [2].

The flow fields of the real human nasal cavities in section V are simulated by a Lattice-Boltzmann Method (LBM) using the Bhatnagar, Gross, and Krook (BGK) [3] approximation. A detailed derivation of the LBM and an extensive discussion can be found in [4].The BGK approximation uses a simplified collision term for the Boltzmann equation leading to the so-called BGK equation without external

forcing which contains the collision frequency, the Maxwell equilibrium distribution function, the particle distribution function, and the components of the molecular velocity vector. That is, the temporal change and the propagation term balance the molecular collisions. The corresponding algorithm is based on the iterative computation of propagation and collision process for each cell of the computational grid. The macroscopic flow variables are determined by summation over the base moments of the distribution function.

Since the LBM formulation is based on uniform Cartesian grid, it is highly adapted for parallel computation and it offers an efficient boundary treatment for fixed walls. The computational grid is automatically generated from arbitrary surface by an in-house grid generator [5]. The ability of reproducing variable organic geometries makes this method well suited for biomedical applications. The standard LBM describes weakly compressible flows and it has been shown in the literature [6] that the LBM yields indeed solutions of the Navier-Stokes equations. More details on the LBM can be found in [7, 8].

III. Discussion of the Unsteadiness of the Flow

To closer examine the unsteady behavior of the nose flow, the complete respiration cycle of the flow through the nasal cavity is numerically analyzed. It is the purpose of this discussion to evidence on the one hand, the differences between steady and unsteady flow solutions at low Reynolds number flows and on the other hand, the extremely good agreement between steady and unsteady flows at high Reynolds numbers. In other words, the analysis shows the steady flow condition to be a valid assumption especially in the high Reynolds number range. Details of the flow fields such as vortices, recirculation regions, and so forth were discussed in [2]. The findings, which address the question whether it is justified to assume the nose flow to be steady and if so, in what Reynolds number range this assumption is justified, are stressed and for this reason the discussion focuses on the macroscopic differences between the flow fields. That is, the comparison of the steady and unsteady solutions is based on juxtaposing pressure loss and wall-shear stress distributions.

III.1. Numerical Setup

III.1.1. Geometry and Mesh

From the data by Masing [9] an anatomically correct replica model with inferior and middle turbinate is constructed. As the superior turbinate is often vestigial in the average human nasal passage it is neglected in this study. That is, we will refer to the anatomical center turbinate as upper turbinate and the inferior turbinate will

be denoted as lower turbinate. The geometry of the nasal cavity model includes besides lower and upper turbinate also cartilage spurs. These are illustrated in the left part of Fig. 1 where the plane section of the septum is not shown to evidence the spurs above the lower and center passage of the cavity.

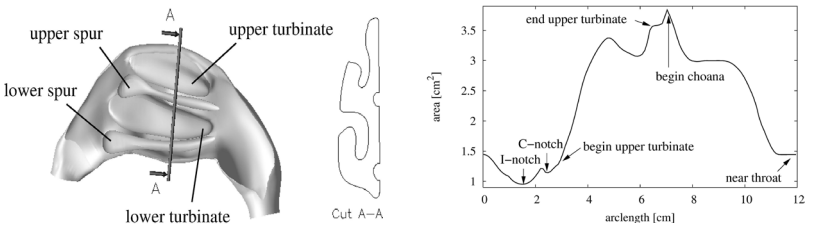

Fig.1: Nasal cavity geometry and coronal cross section (left) and cross section area distribution (right).

Fig. 1 also shows a coronal cross section (left) and an area plot (right) constructed from cross sections normal to a geometrical center line through the cavity. The minimum cross section area is found at the so-called isthmus nasi (I-notch), which is the nasal valve region. The concha notch (C-notch) marks the beginning of the lower turbinate. For normal patients like in the case considered in this study the I-notch is smaller than the C-notch, this is called climbing W. In the case of e.g. an allergic rhinitis the C-notch could have a lower cross section area than the I-notch. Such a distribution of the cross sections would be called descending W [10]. Leading and trailing edge of the upper turbinate are marked separately in the area plot and the beginning of the choana is at the end of the lower turbinate. The area plot evidences the sudden expansion starting at the C-notch.

The grid generation is described at length in [2]. The physical model was scanned using a computer tomograph [11] to obtain an unstructured surface representation by the marching cube algorithm applied to the CT data. The model surface is subdivided into its main components, which are the cartilage spurs at the septum and the turbinates to simplify the grid generation. The resulting structured multiblock grid consists of 32 blocks and a total number of 300,000 cells.

III.1.2. Steady State Boundary Conditions

A no-slip isothermal condition with $T_{wall} = T_\infty$ and a zero pressure gradient normal to the wall are imposed on the wall. Assuming a Strouhal number much smaller than one steady state boundary conditions can be applied at normal respiration. Taking the one-dimensional energy equation for compressible, isentropic flow at the inlet the speed of an isentropic expansion from steady state is given by

$$\bar{w} = \sqrt{\frac{2\kappa}{\kappa - 1}\frac{\bar{p_0}}{\bar{\rho_0}}\left[1 - \left(\frac{\bar{p}}{\bar{p_0}}\right)^{\frac{\kappa-1}{\kappa}}\right]}. \tag{1}$$

The subscript 0 denotes the stagnation state and the quantity $\kappa = 1.4$ is the ratio of specific heats cp/cv for air. This equation is the so-called Saint-Venant/Wanzel equation. Introducing the stagnation state as reference

$$p = \frac{\bar{p}}{\bar{p_0}}, \quad w = \frac{\bar{w}}{\bar{u_0}}, \quad \rho = \frac{\bar{\rho}}{\bar{\rho_0}} \tag{2}$$

and using the ideal gas law equation (1) determines the static pressure at a given expansion velocity

$$p_{new} = \left[1 - \frac{\kappa - 1}{2} p_{old}^{-\frac{2}{\kappa}} (\rho w)^2\right]^{\frac{\kappa}{\kappa-1}}. \tag{3}$$

Equation (3) can be used at the inflow boundary to iteratively compute the static pressure p_{new} at a new time step from the given value of ρw and the pressure value p_{old} from the previous time step. Note that the quantity ρw is an integral value for the inflow cross section such that the actual velocity distribution for the new time step has to be prescribed as an additional condition, i.e., by assuming a fully developed flow.

On the outflow boundary the static pressure level p_∞ is imposed in conjunction with a nonreflecting boundary condition formulation based on a sponge layer [12].

III.1.3. Unsteady Boundary Conditions

It goes without saying that the conditions on the wall, i.e., no-slip, isothermal, and zero normal pressure gradient, still hold in time-dependent flows. To mimic the unsteady flow of the human respiration cycle consider the model sketched in Fig. 2. Inspiration is understood as an isentropic expansion from a steady ambient state with stagnation pressure p_a for the inflow boundary at the nostril. Unlike the discussion in section III.1.2. the outflow boundary, i.e., the boundary just upstream the throat, possesses a time dependent static pressure $p(t) \le p_a = p_\infty$.

At expiration the outflow and inflow boundaries are exchanged. That is, at expiration the throat boundary is the inflow boundary. An isentropic expansion from a steady state is generated through a time dependent stagnation pressure $p_0(t) \ge p_a$ in the throat, whereas a constant pressure $p_\infty = p_a$ is at the nostril.

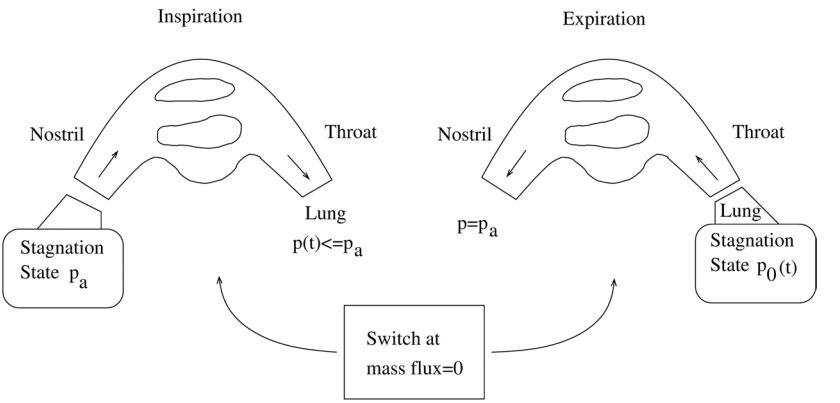

Fig. 2: Scheme for human respiration cycle.

The switching criterion between the inspiration and the expiration phase plays an essential role in the simulation. A possible solution is to switch according to the mass flux

$$\begin{aligned} 0 < |\dot{m}| \leq \triangle\dot{m} \\ \triangle\dot{m}_{in\ to\ ex} = 1.0842\% \cdot \dot{m}_{max.in} \\ \triangle\dot{m}_{ex\ to\ in} = 0.5934\% \cdot \dot{m}_{max.ex} \end{aligned} \tag{4}$$

where $\Delta\dot{m}$ has to be sufficiently small to ensure a smooth and continuous pressure and mass flux change over time during the switching process. Depending on the time step of the flow solver the mass flux also changes discretely. This additionally requires to be larger than the discrete mass flux when the zero mass flux state is approached to smoothly initialize the switch. The chosen values for in this study are given in equation (4). Note that they are different for the transition from inspiration to expiration and vice versa, since the maximum mass fluxes of each phase are different. The shape of the mass flux as a function of time depends on the imposed shape of the pressure distribution over time. Following [13] the unsteady nose respiration has been approximated by a sinusoidal pressure function in this study. Fig. 3 shows the static pressure distributions at the nostril and throat boundary and in addition the mass flux as a function of time. At inspiration the static pressure at the nostril decreases due to the increasing flow velocity, at expiration the fluid flows against the constant pressure p1 of the ambience. The static pressure on the throat boundary is sinusoidal like the prescribed stagnation pressure. The mass flux follows the throat stagnation pressure with a slight time delay, i.e., a small phase shift can be observed when the extrema are juxtaposed.

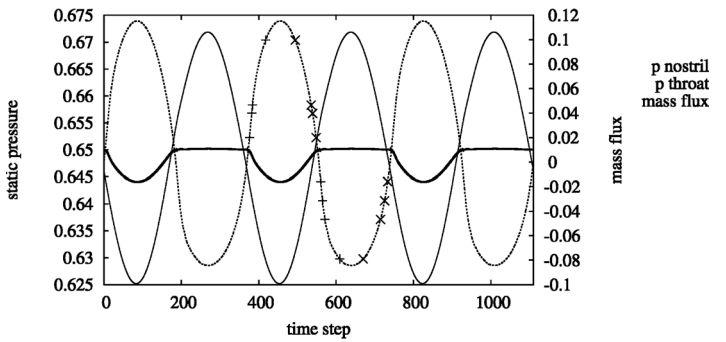

Fig. 3: Static pressure at nostril and throat boundary and mass flux; the symbols represent the time levels t_1(+) and t_2(×) at various Reynolds numbers and mass fluxes respectively.

Note that the maximum mass flux for expiration is lower than that for inspiration which is due to the slower but longer expiration phase at normal breathing conditions.

III.2. Results

The analysis starts by summarizing the main parameters of the steady and unsteady flows to be discussed. Then, a comparison of the total pressure loss over the mass flux of steady state and unsteady results is presented. Next, the skin-friction distribution will be investigated.

The Reynolds numbers and volume fluxes for the steady state simulations of inspiration and expiration are listed in Tab.1 and are based on average normal breathing conditions. It is assumed that the respiratory volume flux is twice that of the single nasal cavity, which is valid for symmetric nasal cavities. The reference length of the Reynolds number is based on the hydraulic diameter d_h = 4A/U = 13.6 mm of the throat, where A represents the area of the cross section and U is the circumference of A. The unsteady flow simulation covers a Reynolds number range $0 \leq Re \leq 2900$ for inspiration and $0 \leq Re \leq 2120$ for expiration. The Strouhal number is $S_r = 0.791$, which emphasizes the unsteady effects and therefore can be deemed a worst-case estimate to check the validity of the steady state assumption. Three respiration cycle periods were simulated. The first period is skipped because of its dependence on the imposed initial flow condition. The second and third period did not show any difference, which is why the further analysis is based on the second period.

In Fig. 4 the unsteady pressure loss as a function of mass flux is presented by the thick solid line. The pressure loss is defined as

$$p_{loss} = \left(p + \frac{\rho}{2}w^2\right)_{nostril} - \left(p + \frac{\rho}{2}w^2\right)_{throat} \quad (5)$$

which permits a smooth curve and yields a negative pressure loss at expiration.

Fig. 4 (left) clearly shows a hysteresis in the pressure loss. The area between the upper and lower curve can be interpreted as power loss of the respiration cycle. The expiration phase possesses a higher pressure loss at large mass fluxes than the inspiration phase. The thin solid line represents a Bezier fit of the averaged unsteady pressure loss over the mass flux. The shape of this line is in good qualitative agreement with the pressure curves presented in [14]. The results of steady state flows at several Reynolds numbers are given by the crosses. It is evident that there is an excellent agreement between the averaged unsteady and the steady state results. This makes sense since the steady state represents a Strouhal number limit of zero in which case the unsteady thick solid line will approximate the thin solid curve of the Bezier fit. The lower the Strouhal number the less hysteresis will occur. Also note that when the mass flux decreases in the inspiration and expiration phase the unsteady results are closer to the steady state solution. This observation will be confirmed by the following discussion.

Re	$\dot{q}_{single}$ *(ml/s)*	$\dot{q}_{respiration}$ *(ml/s)*	$\dot{q}_{respiration}$ *(ml/min)*	state
500	79.6	159.2	9.6	
1000	159.2	318.3	19.1	inspiration
1170	186.2	372.4	22.4	
2500	397.9	795.8	47.8	
400	63.7	127.3	7.6	
790	125.7	251.5	15.1	expiration
1170	186.2	372.4	22.4	
1980	315.1	630.3	37.8	

Table 1: Reynolds numbers and volume fluxes for steady state simulations.

Fig. 4 (right) shows distributions of the static pressure vs. mass flux based on rhinomanometry measurements [15]. A pipe-shaped nose model having a diameter of d = 6 mm and a length of l = 100 mm is used at 44 and 88 respiration cycles per minute. The lower respiration frequency is illustrated in quadrant I and III and the higher frequency in quadrant II and IV. The measurements confirm two major results discussed above. First, the shape of the distribution visualizing the

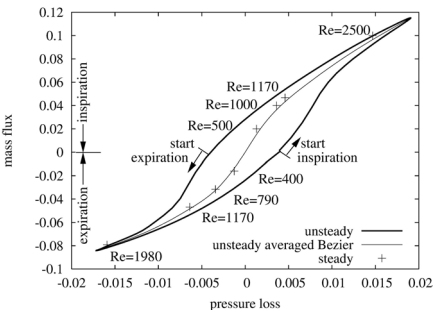

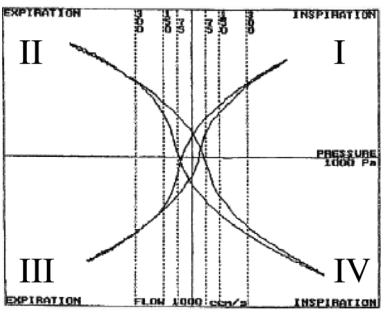

Fig. 4: Pressure loss vs. mass flux, comparison of steady state and unsteady results (left). Note due to the pressure loss definition given by Eqn. (5) negative pressure loss values can occur. Rhinomanometry measurement of static pressure vs. mass flux of a pipe-shaped nose model [15](right).

fact that at high Reynolds numbers or in other words, at high mass fluxes the nasal cavity flow can be assumed steady. Second, the tendency to reduce the hysteresis at lower frequencies. This trend has been described above when the steady state simulations have been discussed.

The further analysis is based on comparisons of Re = 500, Re = 1170 at inspiration and Re = 400, Re = 1170 at expiration. The results for Re = 1000 and Re = 790 are similar to those at Re = 1170 which is why they are skipped in this analysis. At Re = 2500 and Re = 1980 steady and unsteady flow results coincide since there is hardly any hysteresis at such high mass fluxes. Therefore, these results are not addressed in the following discussion. Due to the hysteresis the steady state results are compared with unsteady findings having the equivalent intermediate Reynolds number. To enable a direct comparison analogous scales are used for the steady and unsteady results.

In the following, the wall shear stress, i.e., the skin-friction distributions are compared. This quantity can be considered to indicate through high values areas endangered of dryness of the mucosa. All solutions presented in Figs 5 and 6 possess high wall shear stress in the region of the nasal valve and the tip of the lower turbinate and lower septum spur. In other words, the flow in the sudden expansion area at the nasal valve does not strongly depend on the temporal changes of the respiration cycle. This is different when the entire surface is considered. At inspiration an area of high skin friction can be observed on the upper turbinate. The extent of this area undergoes a large variation from covering the complete lower edge at the steady state solution Re = 1170 and the distribution for the unsteady computation Re(t2) = 1170 to the non-existence of this area for the unsteady solution at the increasing mass flux Re(t1) = 500. Furthermore, there is also high wall shear stress in the olfactory region for the steady and unsteady

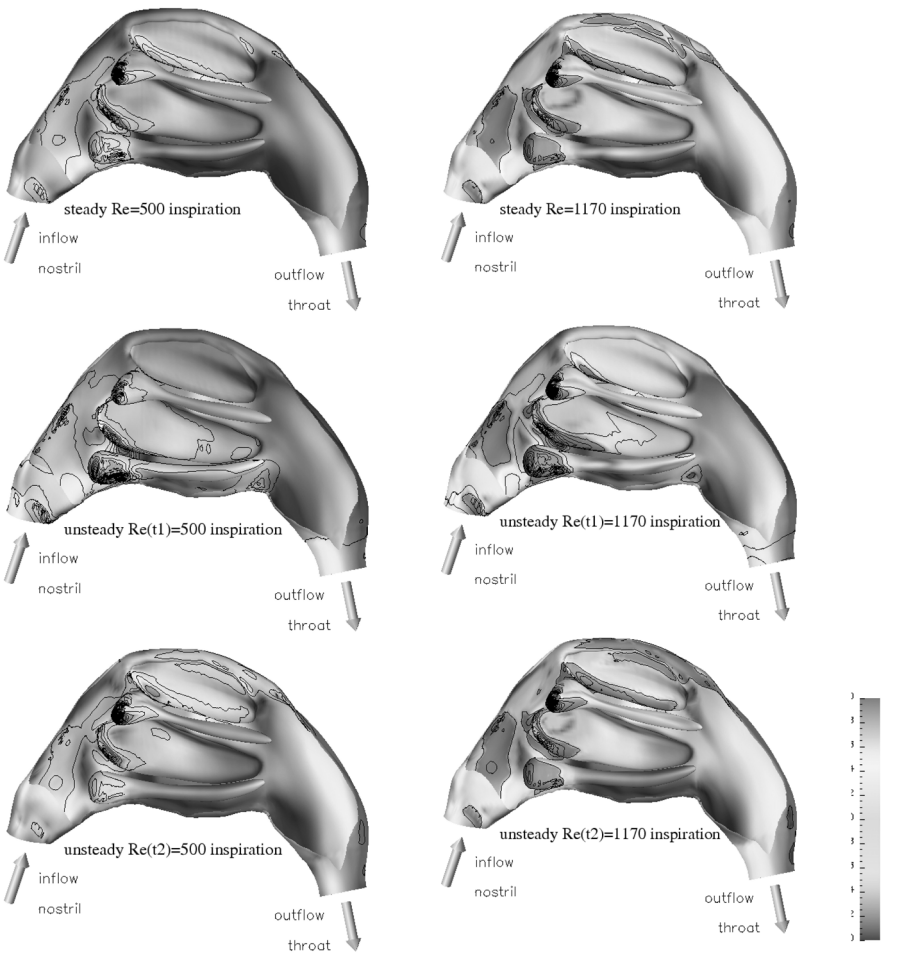

Fig. 5: At Re = 500 (left) and Re = 1170 (right) wall-shear stress distributions are compared for steady and unsteady flows at inspiration.

solutions at Re = 1170, Re(t2) = 1170, and Re(t2) = 500. Again, the best match occurs between the steady Re = 1170 and the unsteady Re(t2) = 1170 solutions, whereas the worst match is obtained for the steady and unsteady solutions, i.e., at Re = 500 and Re(t1) = 500. At expiration shown in Fig. 6 the area of high skin friction on the lower edge of the upper turbinate is not observed. It is interesting to note that the overall resemblance of the wall shear stress distributions between the steady state and unsteady results is definitely better for the expiration than for

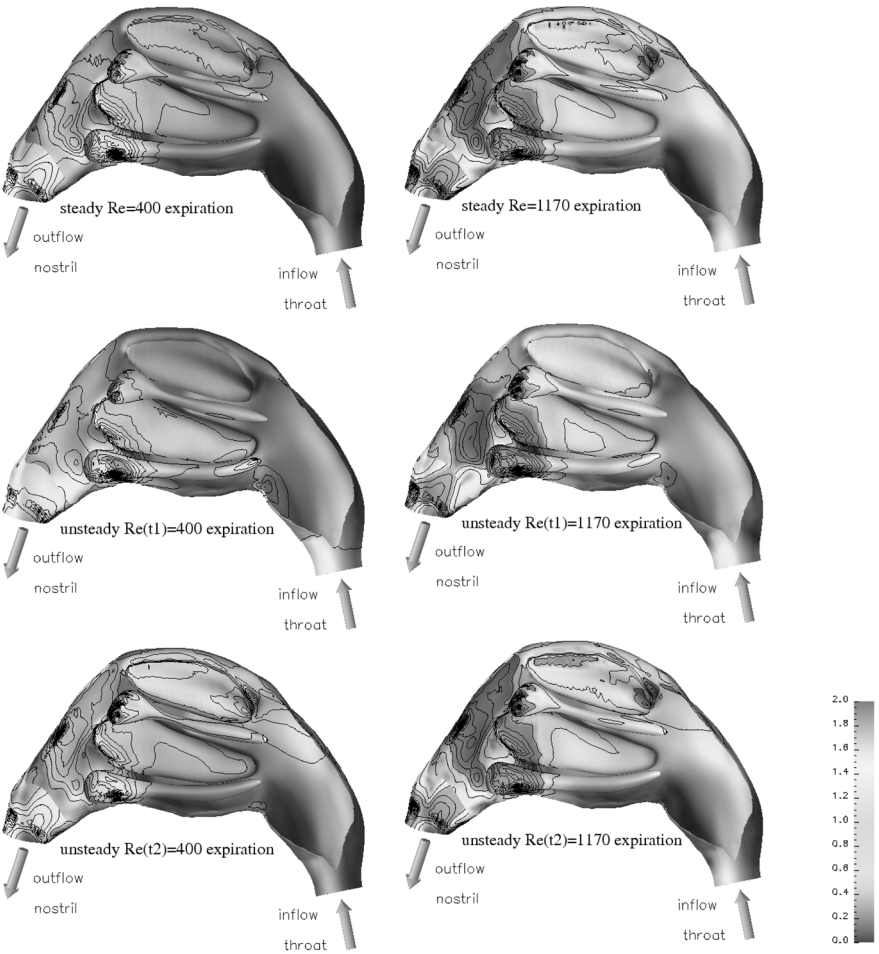

Fig. 6: At Re = 400 (left) and Re = 1170 (right) wall-shear stress distributions are compared for steady and unsteady flows at expiration.

the inspiration phase. That is, the near-wall flow field seems to be less susceptible to cyclic changes at expiration than inspiration.

In brief, a detailed analysis of the unsteady respiration cycle through a model of the human nasal cavity was performed at Sr = 0.791. The comparison of the steady state and unsteady solutions showed the major differences to occur at increasing mass flux. At decreasing mass flux only small discrepancies between the steady and unsteady findings were observed. Near transition between inspiration

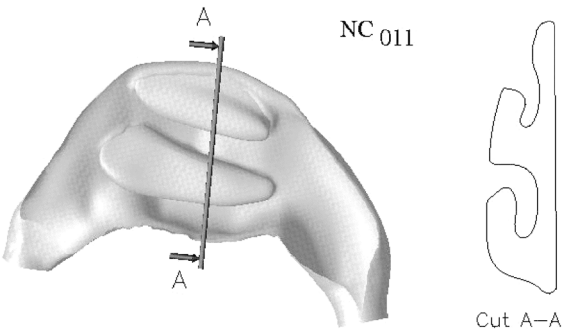

Fig. 7: Model of the nasal cavity with upper and lower turbinate.

and expiration, i.e., at small mass fluxes the unsteady results are fundamentally different from the steady state solutions. However, at high mass fluxes the characteristic features of the nasal cavity flows are well captured by the steady state solutions. From this analysis it could be stated as a rule-of-thumb that at Sr $\approx$ 0.8 it is appropriate to assume the nasal cavity flow to be steady if the Reynolds number satisfies Re > 800.

IV. Discussion of the Flow State

Most of the investigations published in the literature are performed under the assumption that the flow in the human nasal cavity it turbulent. Considering, however, the variation of the geometry of the nasal cavity this assumption is quite brute force. It is more likely that a locally intermittent flow state exists or a well-resolved laminar flow captures the essential flow physics. To show the relevance of this statement, we compare experimental and numerical results for a model geometry which is illustrated in Fig. 7. The numerical method is based on the aforementioned structured finite-volume flow solver. The boundary conditions were also discussed above. Before the discussion of the results, the experimental setup will be described.

IV.1. Experimental Method

To measure the velocity distribution the method of Digital Particle-Image Velocimetry (DPIV) is used. The application of this optical method requires a fully unobstructed view into the inner flow region, i.e., a completely transparent model of the nasal cavity and an appropriate fluid with the same optical refractive

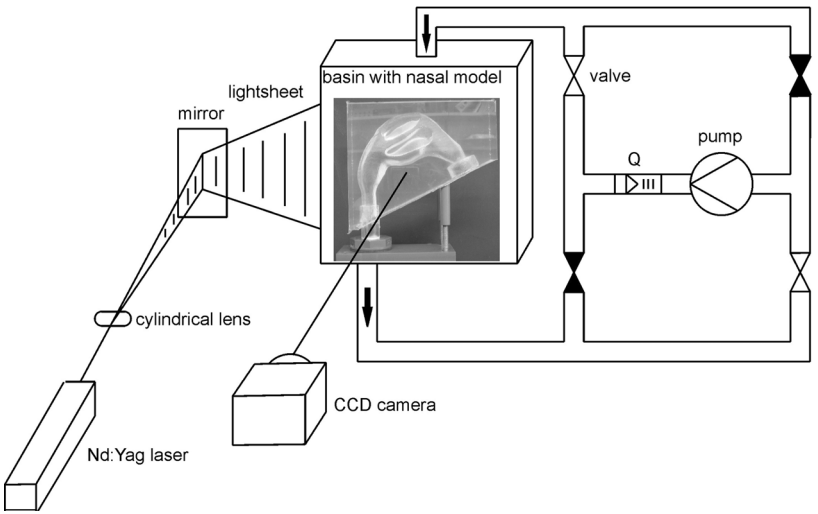

Fig. 8: Principal sketch of the DPIV setup and the optical arrangement for measurements in sagittal planes parallel to the septum.

index as the material of the model. In previous studies we used a model made of epoxy-based cast resin and the fluid tetraline [16]. Due to the complex handling of tetraline and the relatively high refractive index of epoxy-based resin, we apply an alternative method described by Hopkins et al. [17], i.e., we use a rapid-prototyping process to manufacture a nose model made of silicone.

Owing to the small size and complex geometry of the human nasal cavity a 1.5-scaled model was built. The geometry was taken from the previously described CT-scans and stored as an STL data file. This is a common format for machining tools or rapid prototyping and it describes the 3-D surface as an unstructured grid. From these data a "negative" kernel of the nasal passage is generated with rapid prototyping. The material is a water soluble cornstarch, which is glued layer by layer in a 3-D printing device. The corresponding positive is obtained by casting the kernel in a transparent silicone block. After curing the kernel is washed out yielding a silicone block with the nasal passage as internal flow geometry.

The model is placed within a flow loop with water/glycerol as carrier medium (Fig. 8). The complete model is fully immersed within a squared basin made of acrylic glass to which the inflow and outflow devices are connected. The inlet of the nostril region possesses the shape of a smooth nozzle being connected to the container box. The flow through the nasal cavity exits into the throat, which is simulated by a long straight pipe. The refractive index of the silicone matches that of a volume ratio mixture of glycerol to water of 55%. The mass flow rate

is adapted to the characteristic air flow parameters in the nose by keeping the Reynolds number constant. Inspiration and expiration are produced by changing the flow direction in the pipe system.

The hydrogen bubble technique is used to produce fine air bubbles as tracer particles, which are recorded by the CCD camera to visualize and quantitatively measure the flow. For the DPIV measurements the fluid is illuminated in planar laser light sheets generated by a double pulse Nd:YAG laser. The light sheets are arranged in sagittal planes parallel to the septum and in coronal cross-sections of the nasal passage. The 20 sagittal planes are 1 mm apart and 10 coronal planes cover the flow between the nostril and the throat. All measurements are taken with a single DPIV camera. Since this study focuses on the investigation of the mean flow behavior, i.e., the mean velocity profiles and complex flow patterns such as vortex structures or separation areas, the results are based on an average of 50 DPIV recordings.

IV.2. Results

At inspiration and expiration we assume volume fluxes for respiration at rest of 159.15 ml/sec and 127.32 ml/sec that result in Reynolds numbers of Re = 500 and Re = 400, respectively. Note that in this study the mean Reynolds number based on the mean channel width for the highest considered volume flux of 318.31 ml/sec is in the range of 1030 to 1400 for all configurations investigated, which is why the flow in the numerical analysis is conjectured laminar. The reference length for the Reynolds number is based on the hydraulic diameter of the throat. Furthermore, as aforementioned the flow can be considered steady since the Strouhal number is much smaller than one.

In Figs 10–13 numerical and experimental findings are juxtaposed at inspiration and expiration. For comparison reasons all results are interpolated on equidistant orthogonal grids. The locations of the four selected sagittal and coronal cross sections are indicated in Fig. 9. The cross sections were chosen such that they are in areas, where highly susceptible flow features, e.g., jet-wall interactions, single and double vortices, occur to make the experimental and numerical comparison more reliable. In Fig. 10 cross section 1 shows the flow over the lower and upper turbinate at inspiration. Upstream of the upper turbinate a small vortex-like structure occurs, which is detected by the simulations and the experiments. The cross sections 2–4 in Fig. 10 present mainly the deflection of the flow by the lower and upper turbinate. A closer look reveals a good agreement as far as the angle and the magnitude of the velocity vectors are concerned. Fig. 11 contains the velocity distribution at expiration. The visualization in cross section 1, which shows the flow field between the septum and the turbinates, evidences the same overall flow orientation in the computed and the measured distributions. The cross

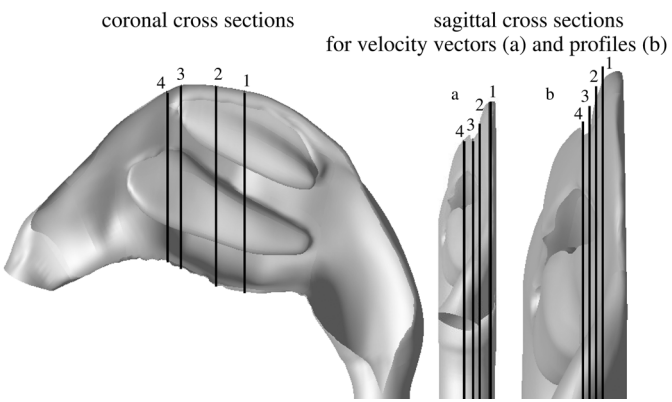

Fig. 9: Positions of coronal (left) and sagittal (center and right) cross sections.

sections 2–4 exhibit a jet-like flow downstream of the throat that interacts with the outer boundary of the nasal cavity upstream of the upper turbinate. The flow structure in the vicinity of the interaction area does coincide in the numerical and the experimental findings. The same statement holds when the flow in the channel between the upper and lower turbinate, below the lower turbinate, and in the area downstream of the lower turbinate and upstream of the nostril are considered. Therefore, it is fair to conclude, that a convincing experimental and numerical agreement is proven by the velocity distributions in the sagittal cross section in Figs 10, 11. Furthermore, the comparison of Figs 10, 11 emphasizes the mixing character of the flow at inspiration and the jet-like character at expiration.

In Figs 12, 13 the velocity distributions at inspiration and expiration in several coronal sections are shown, where cross section 1 is closest to the throat and cross section 4 is nearest the nostril region (Fig. 9). In Fig. 12 there is a double vortex structure visible between the lower and upper turbinate in cross sections 1 and 2. The qualitative agreement between the computations and measurements is definitely good in the cross section near the throat. A slight discrepancy occurs in cross section 4 since the vortex structure above the lower turbinate is not observed before cross section 3 in the experiments whereas the numerical analysis reveals such a vortical structure already in cross section 4. When the less intricate flow region below the lower turbinate is considered, again a satisfactory correspondence between numerics and measurements is visualized. At expiration a strong flow from the region between the upper and lower turbinate through the area between the lower turbinate and the septum is evidenced in cross sections 1 and 2 in Fig. 13. Closer to the nostril, i.e., in cross sections 3 and 4, a converging flow structure with a separation line on the septum is determined in almost the same location in the numerical and experimental findings.

To summarize, the results in Figs 10, 11, 12, and 13 show the good agreement of the computations and the measurements in the sagittal and coronal cross sections and prove the numerical method and the laminar flow assumption to yield the proper description of the overall flow structure.

V. Comparison of the Flow Fields of Three Real Noses

It goes without saying for any useful computed aided surgery (CAS) concept it is a must that real human geometries, e.g., nasal cavities, can be numerically represented and that the flow field can be simulated at such an accuracy that the essential differences which are due to the flow parameters and the geometric intricacy can be resolved. To show that these prerequisites for a promising CAS approach are satisfied an analysis of the flow field of three different nasal cavities is given next.

The numerical method is based on a Lattice-Boltzmann formulation that was briefly sketched in section II. The boundary conditions are similar to those discussed in the beginning of section III.

The three geometries, i.e., the nasal cavities, are labeled good, medium, and poor (N_g, N_m, N_p). This classification is based on a personal evaluation of the patient, who filled out a questionnaire related to his respiration impression, and a validation by rhinologists. More details on the geometries, the numerical method, the mesh, and the postprocessing of the data can be found in [18].

The discussion of the results will focus on the vortical flow structures, the wall shear stress, and the heat flux distribution. Further findings are discussed in [18]. Note that only the steady inhalation has been simulated.

V.1. Results

V.1.1. Vortical Flow Structures

To analyze the mixing process in the various geometries the vortical flow structures will be discussed. First, a thorough investigation is presented for the good nasal cavity N_m, which shows a production of unsteady frequently shed secondary flow structures in the wake region of the turbinates. Then, the less pronounced flow structures in the poor and good geometries N_p and N_g are described.

It is clear from the illustration shown in Fig. 14b that in the configuration N_m the flow is accelerated near the nostrils in the nasal valve. This phenomenon is due to the converging channel in this region and was also observed in [19, 20]. Upstream of the swollen turbinates the flow is homogeneously distributed in the left and right cavity. In the left cavity the flow is split by the lower turbinate. Partially, the fluid is directed through the small lower channel, which causes a local

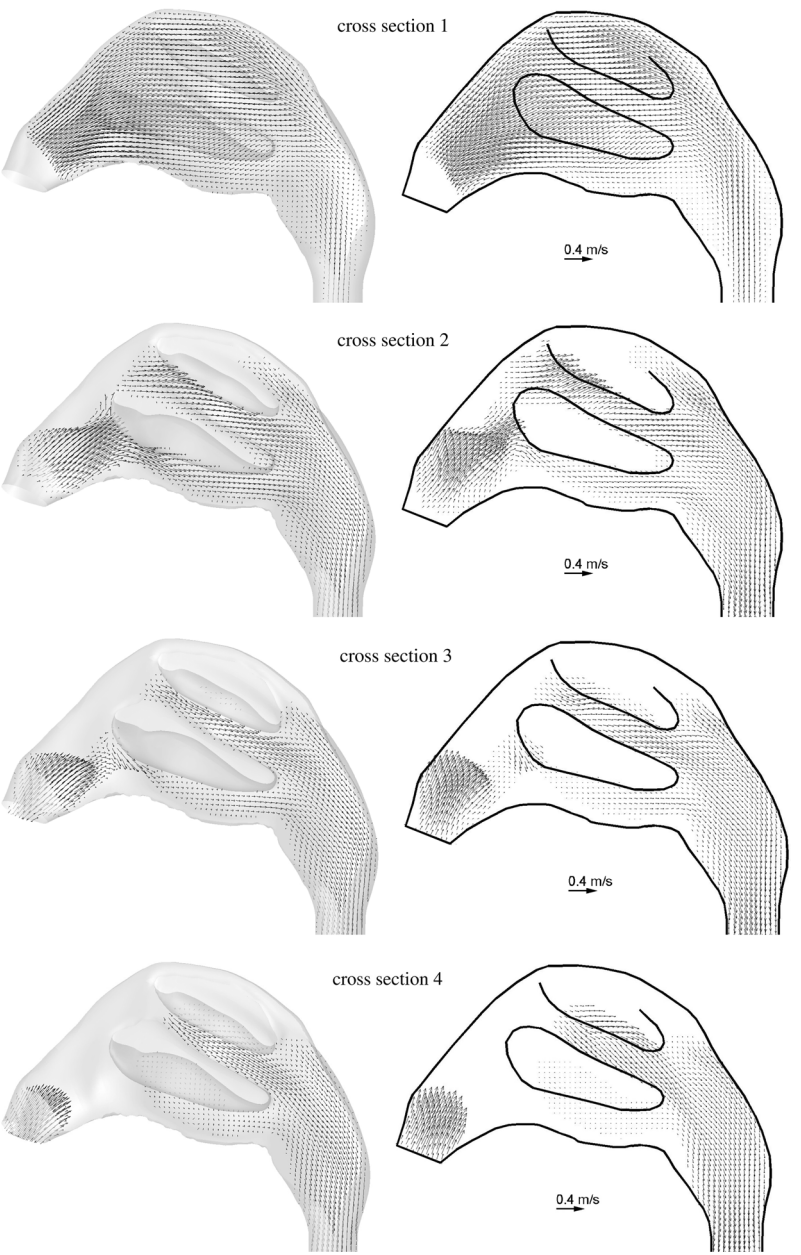

Fig. 10: Velocity field in several sagittal cross sections at inspiration (Re = 500); comparison of numerical (left) and experimental (right) results.

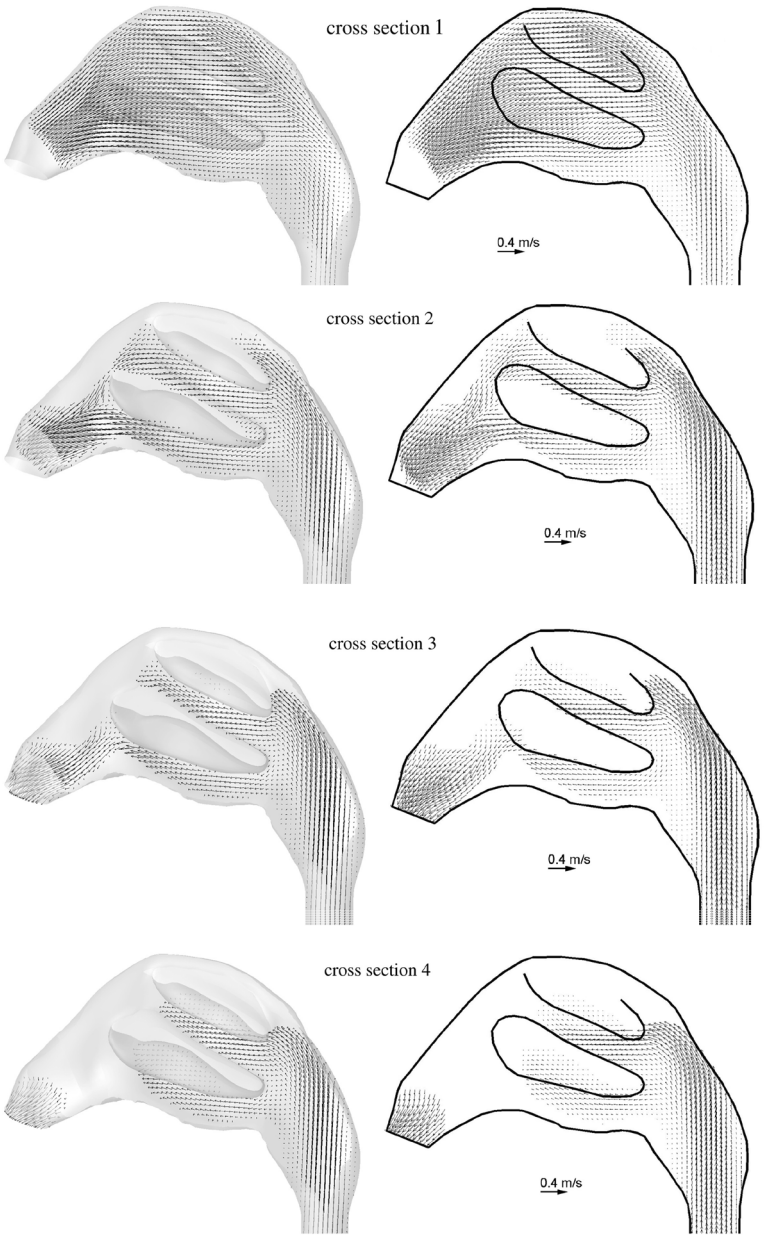

Fig. 11: Velocity field in several sagittal cross sections at expiration (Re = 400); comparison of numerical (left) and experimental (right) results.

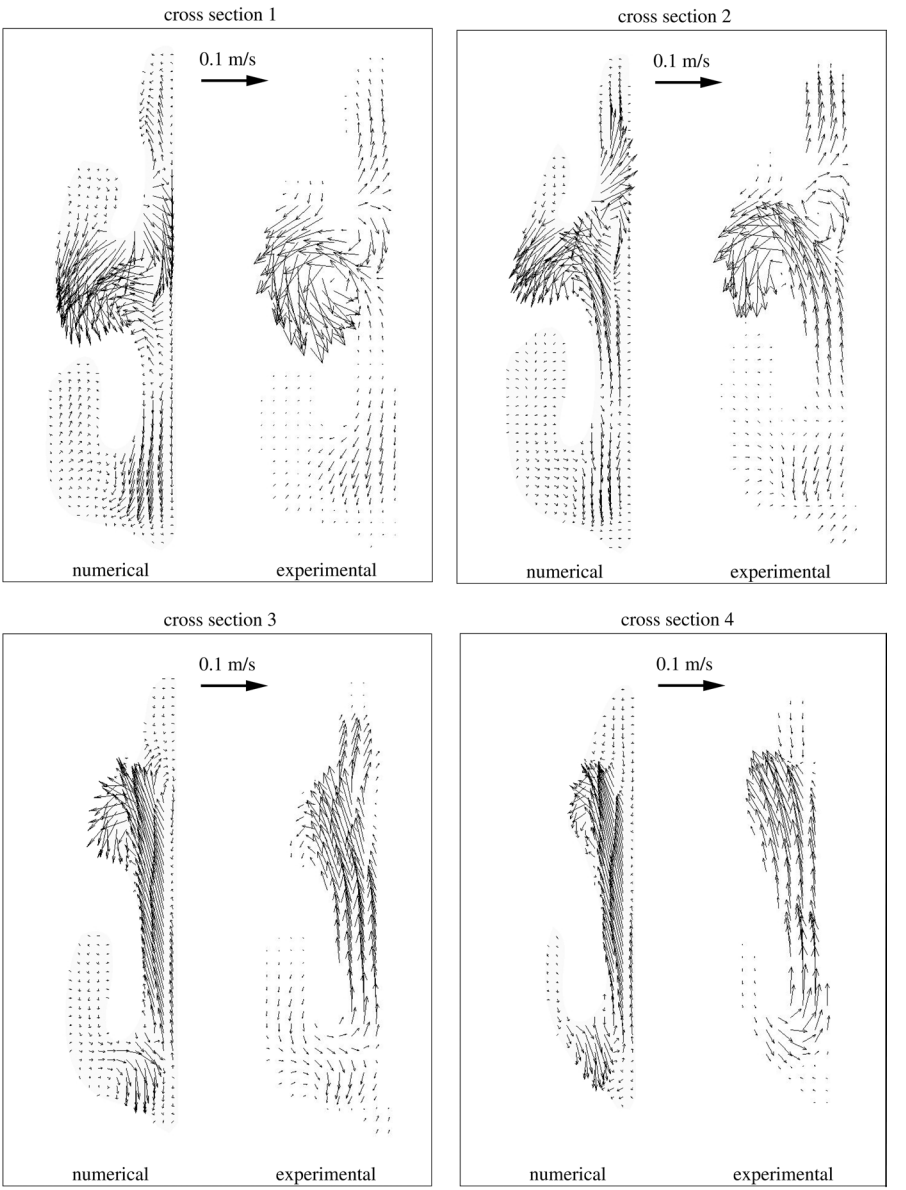

Fig. 12: Velocity field in several coronal cross sections at inspiration (Re = 500); comparison of numerical (left) and experimental (right) results.

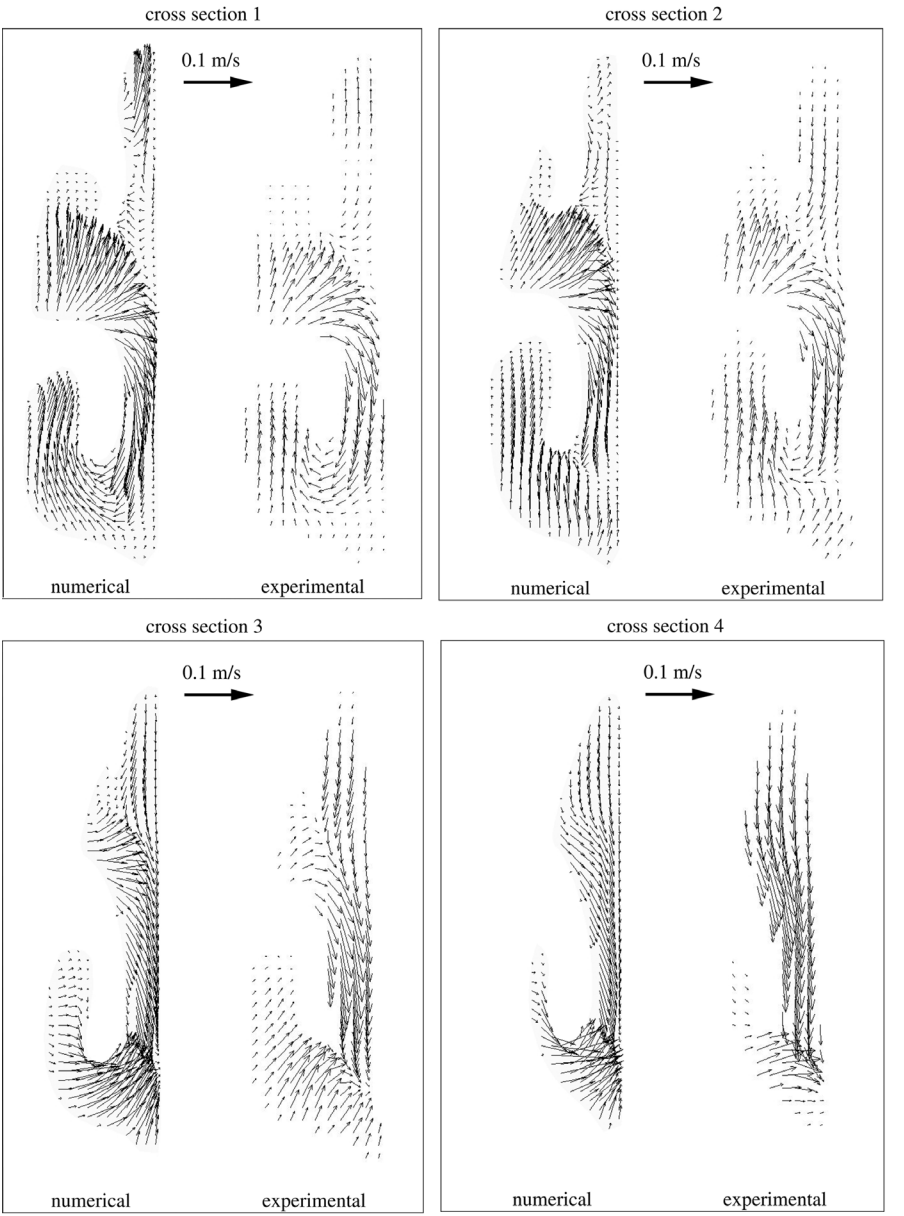

Fig. 13: Velocity field in several coronal cross sections at expiration (Re = 400); comparison of numerical (left) and experimental (right) results.

velocity increase. The fluid exits the turbinate channels in a region dominated by mixing jets, which causes the production of unsteady frequently shed secondary flow structures.

The streamlines colored by the velocity magnitude in Fig. 14c evidence the major impact of the missing left center turbinate in the nasal cavity N_p on the overall flow structure. The flow is accelerated near the nostril in the nasal valve and directly guided towards the back of the nasal cavity. The flow performs a clockwise rotation about the streamwise axis before forming a recirculation zone caused by the interaction with the backwall of the cavity. Most of the fluid is deflected towards the pharynx, where the left and right cavity merge. Due to the geometric shape, the flow rotates about the streamwise axis. The side views show the fluid to enter the paranasal sinus and to form a vortex in this region. The part of the fluid in the nasal cavity is accelerated by the converging channel in the pharynx. The septum perforation causes a direct interaction of the flow fields in the left and the right cavity in the region of the missing lower turbinate, where a slowly tumbling recirculation zone is formed (Fig. 14c).

A comparison of the streamlines colored by the velocity magnitude in the side views of the configuration N_g in Fig. 14a shows the flow in the left cavity to be uniformly distributed, whereas the major flux in the right cavity is located in the region of the lower and center turbinate. The homogeneous distribution of the flow in the entire left cavity is based on the low velocity, which increases at the end of the turbinates. Unlike the streamwise velocity gradient in N_p and N_m the acceleration of the fluid into the pharynx is small.

V.1.2. Wall-Shear Stress

Fig. 15 shows the dimensionless wall-shear stress distributions $\tau_w = \overline{\tau}_w / \overline{\tau}_{w,\lambda}^{max}$ of the configurations N_g, N_m, and N_p. Note that for better visualization, the paranasal sinuses are removed. The comparison evidences the Ng configuration to have a smoother distribution than the configurations N_m and N_p. That is, only some local maxima are observed in regions of converging channels, i.e., in the left nasal cavity close to the nostril and in both cavities upstream of the pharynx entrance.

The N_m configuration is dominated by regions of high wall-shear stress τ_w. The overall smaller channel width leads to a higher mean flow at a comparable mass flux resulting in a higher wall shear. The smaller cross section close to the nostrils also leads to a local maximum. The strong septum deviation and the swollen lower turbinate result in high wall-shear stress in the right nasal cavity. In the left cavity, the fluid impinges upon the lower turbinate resulting in a local maximum. The major increase occurs in the pharynx, where the flow from both sides merges into a mixing zone. The highest shear stress is reached at the back of the pharynx, where the fluid is guided downstream to the larynx.

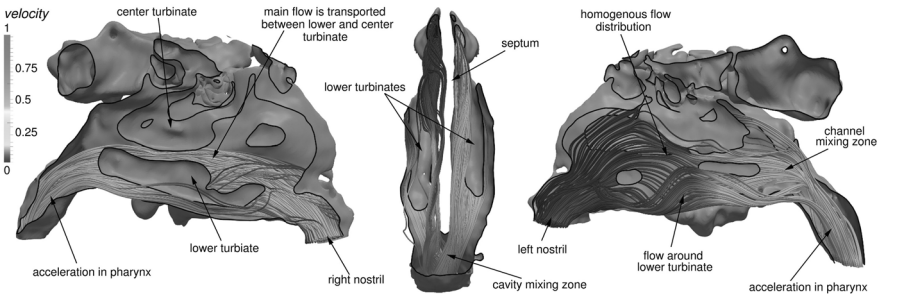

a) Streamlines in the nasal cavities N_g.

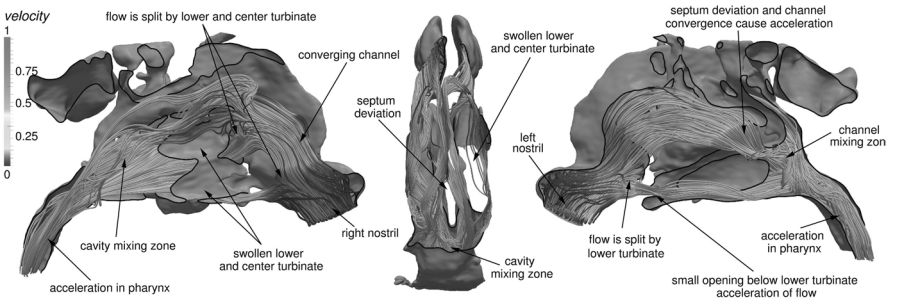

b) Streamlines in the nasal cavities N_m.

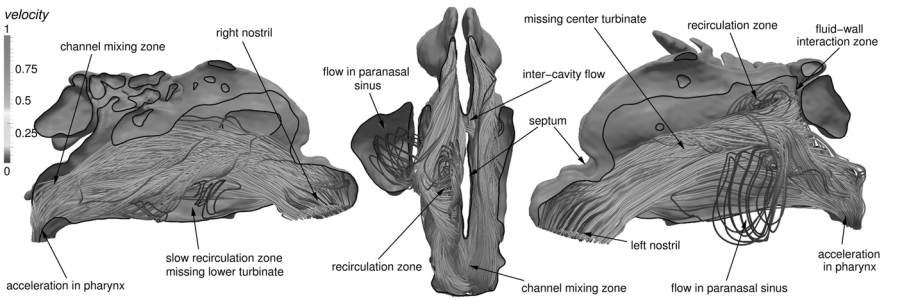

c) Streamlines in the nasal cavities N_p.

Fig. 14: Streamlines in the nasal cavities N_g, N_m, and N_p colored by the velocity magnitude $v_r = \overline{v}/\overline{v}_{max}$, where $\overline{v}_{max}$ = 6.5 m/s the maximum dimensional velocity of all configurations. Side views (left and right column) and top views (center column) of the three-dimensional geometries are shown.

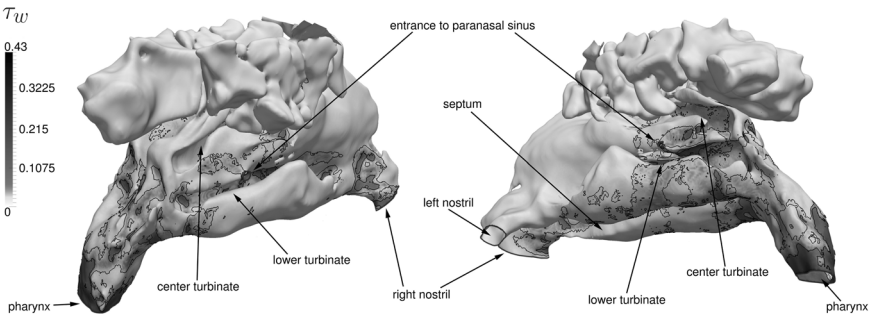

a) Wall-shear stress distribution τ_w in the nasal cavity configurations N_g.

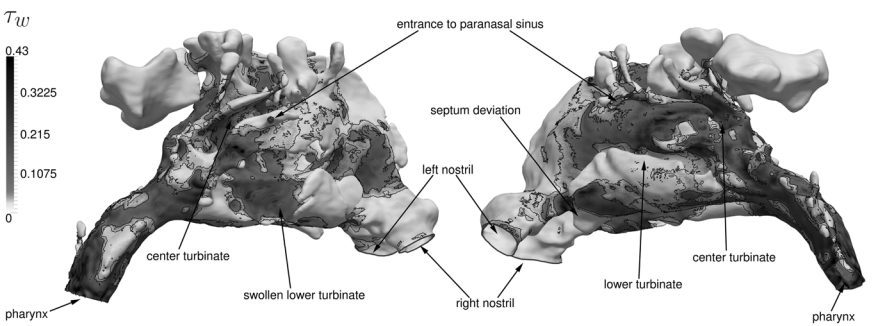

b) Wall-shear stress distribution τ_w in the nasal cavity configurations N_m.

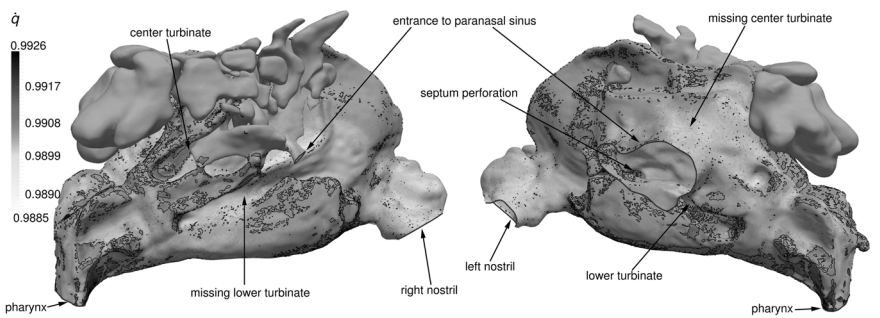

c) Wall-shear stress distribution τ_w in the nasal cavity configurations N_p.

Fig. 15: Wall-shear stress distribution τ_w of the various nasal cavity configurations N_g, N_m, and N_p. The paranasal sinuses were removed for better visualization.

Like N_g and N_m the configuration N_p also possesses local maxima near the nostrils. In the left nasal cavity the fluid interacts with the outer backwall causing the increased wall-shear stress downstream of the large orifice to the paranasal sinus. This flow behavior occurs since the center turbinate is removed and the fluid is directed against the nasal cavity wall. The septum perforation experiences an increased τ_w due to the mass flow from the left to the right nasal cavity. In the right nasal cavity the fluid enters a converging channel in the region of the center turbinate, which is why this region is dominated by increased wall-shear stress. Downstream of the turbinates a ring of high τ_w is formed due to the converging-diverging channel geometry. However, the highest wall-shear stress is again determined further downstream in the pharynx.

V.1.3. Heating Capability

To complement the evaluation of the respiration efficiency of the nasal cavities the dimensionless heat flux distribution for the three configurations N_g, N_m, and N_p is shown in Fig. 16. Note that $\dot{q}$ is normalized by its maximum over all configurations $\dot{q}_{max?}$. The juxtaposition of the distributions shows that the heat flux is best in the sense of smoothly increasing in configuration N_g (Fig. 16a). Especially in the right nasal cavity, $\dot{q}$ continuously increases along the streamwise direction. In contrast to the left side $\dot{q}$ is almost equally distributed between the turbinate channels. The major heat flux occurs in the retral part of the turbinate channels and the pharynx.

The distribution in configuration N_m in Fig. 16b is dominated by local maxima in the retral part of the turbinate channels. A smooth distribution is determined in the lower turbinate channel of the left nasal cavity in the channel mixing zone of the right cavity, and in the pharynx region. However, the overall $\dot{q}$ distribution is decreased compared to configuration N_g. The low heat flux distribution of configuration N_p in Fig. 16c emphasizes the low heating capability of this nasal cavity.

VI. Conclusion

The fluid mechanics of model and real nasal cavities has been numerically analyzed by a finite-volume and a Lattice-Boltzmann method. It has been the flow physics not the numerics that has defined the core of the discussion.

First, the flow through a model has been analyzed at a Strouhal number $Sr = 0.791$ for the complete unsteady respiration cycle. For validation purposes the findings have been compared with steady state solutions for inspiration and expiration. From the comparison of the steady state and unsteady solutions it can be stated as a rule-of-thumb that at $Sr \approx 0.8$ it is appropriate to assume the nasal cavity flow to be steady if the Reynolds number satisfies $Re > 800$.

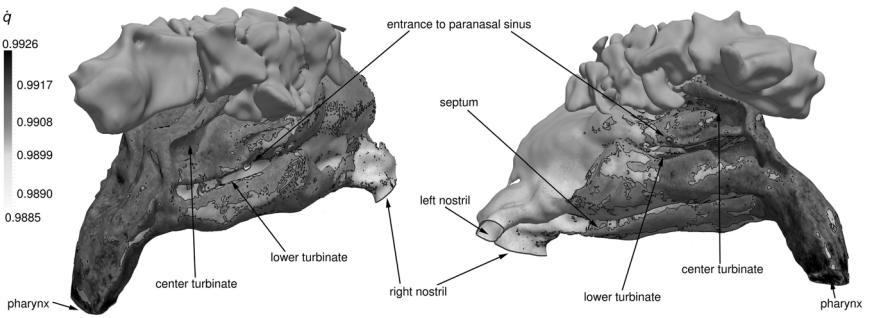

a) Heat flux $\dot{q}$ in the nasal cavity N_g.

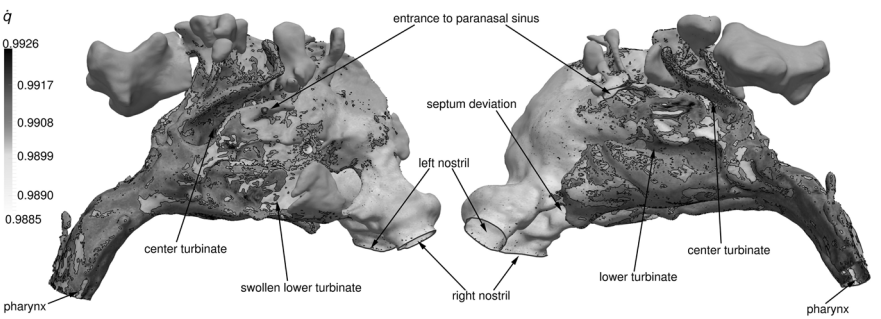

b) Heat flux $\dot{q}$ in the nasal cavity N_m.

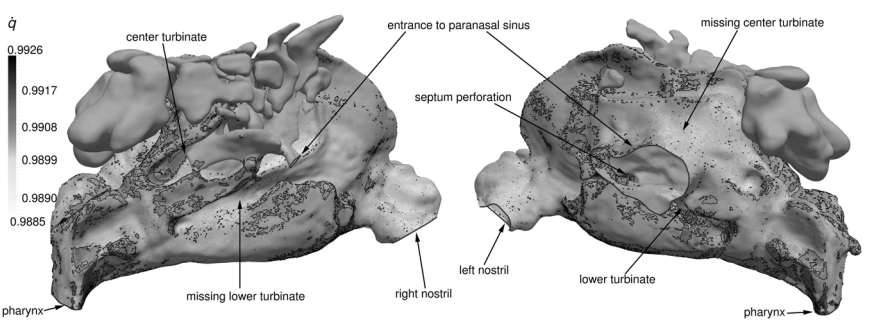

c) Heat flux $\dot{q}$ in the nasal cavity N_p.

Fig. 16: Heat flux distribution $\dot{q}$ of the various nasal cavity configurations N_g, N_m, and N_p. The paranasal sinuses were removed for better visualization.

Next, results for flow simulations and experiments have been presented to discuss the flow state. The experimental results have corroborated the numerical flow structures which have been determined without any turbulence model, thereby evidencing that the nose flow can be considered laminar.

Finally, the analysis of three real nasal cavities has shown that the removal of turbinates yields a lower total drag such that less energy is necessary to inhale. However, the heating capability is lower compared to the other configurations due to the reduced surface area. The local wall-shear stress is highest in the poor configuration resulting in an increased potential inflammation load. The septum bending and the swollen turbinates in the medium configuration lead to the highest averaged wall-shear stress. The heating capability is best for the medium geometry although the surface area and the overall heat flux distribution is smaller than that of the good configuration. However, the heating capability is strongly dependent on the flow distribution and does not necessarily correlate with the surface area and the heat flux distribution. The good configuration possesses a slightly lower heating capability and the averaged wall-shear stress distribution is lowest.

Literature

[1] Fares, E., M. Meinke and W. Schröder 2000: Numerical Simulation of the Interaction of Wingtip Vortices and Engine Jets in the Near Field. AIAA Paper 2000–2046.

[2] Hörschler, I., C. Brücker, W. Schröder and M. Meinke 2006: Investigation of the Impact of the Geometry on the Nose Flow. European Journal of Mechanics-B/Fluids **25**(4), 471– 490.

[3] Bhatnagar, P.L., B.P. Gross and M. Krook 1954: A Model for Collision Processes in Gases. I. Small Amplitude Processes in Charged and Neutral One-Component Systems. Phys Rev **94**(3), 511–525.

[4] Benzi, R., S. Succi and M. Vergassola 1992: The Lattice Boltzmann Equation: Theory and Applications. Physics Reports **222**(3), 145–197.

[5] Hartmann, D., M. Meinke and W. Schröder 2008: An adaptive multilevel multigrid formulation for Cartesian hierarchical grid methods. Comput. Fluids **37**, 1103–1125.

[6] Hänel, D. 2004: Molekulare Gasdynamik. Springer: Berlin, 2004.

[7] Freitas R.K. and W. Schröder 2008: Numerical investigation of the three-dimensional flow in a human lung model. Journal of Biomechanics **41**, 2446–2457.

[8] Eitel-Amor, G., M. Meinke and W. Schröder 2013: A Lattice Boltzmann method with hierarchically refined meshes, Comp. Fluids **75**, 127–139.

[9] Masing, H. 1967: Experimentelle Untersuchungen über die Strömung im Nasenmodell. Archiv klin. exp. Ohren-, Nasen- u. Kehlkopf-Heilk. **189**, 59–70.

[10] Pallanch, J.F., T.V. McCaffrey and E.B. Kern 1998: Otolaryngology – Head and Neck Surgery (Eds. C.W. Cummings and J.M. Fredrickson and L.A. Harker and C.J. Krause and M.A. Richardson and D.E. Schuller), chapter 42 Evaluation of Nasal Breathing Function with Objective Airway Testing, 799–832. Mosby, St. Louis, 3rd edition.

[11] Hentschel, B., T. Kuhlen and C. Bischof 2005: VRhino II: Flow Field Visualization inside the Human Nasal Cavity. In Proceedings of the IEEE Virtual Reality 2005, 233–236, Bonn, Germany, March 12–16.

[12] Colonius, T. 1997: Numerically nonreflecting boundary and interface conditions for compressible flow and aeroacustic computations. AIAA Journal, **35**(7), 1126–1133.

[13] Hincliffe, R. and D. Harrison 1976: Scientific Foundation of Otolaryngology, 502–512, William Heinemann Medical Book LTD, London.

[14] Schreck, S., K.J. Sullivan, C.M. Ho, and H.K. Chang 1993: Correlations between flow resistance and geometry in a model of the human nose. J. Appl. Physiol. **75**, 1767–1775.

[15] Vogt, K. and H. Hoffrichter 1993: Neue strömungsphysikalische Erkenntnisse in der Rhinomanometrie und ihre praktischen Konsequenzen. In: Topische Therapie der allergischen Rhinitis (Eds. Mösges, Schlöndorff). 45–60, Biermann Verlag, Germany,

[16] Brücker, C. and K.I. Park 1999: Experimental study of velocity fields in a model of human nasal cavity by DPIV. In Proc. 1st Int. Symp. Turbulence and Shear Flow Phenomena (Eds. Banerjee, S. and K. Eaton), 831–836. Santa Barbara, California, Sept. 12–15.

[17] Hopkins, L., J. Kelly, A. Wexler and A. Prasad 2000: Particle image velocimetry in complex geometries. Experiments in Fluids **29**, 91–95.

[18] Lintermann, A., M. Meinke and W. Schröder 2013: Fluid mechanics based classification of the respiratory efficiency of several nasal cavities, submitted to Computers in Biology and Medicine.

[19] Yu, S., Y. Liu, X. Sun and S. Li 2008: Influence of nasal structure on the distribution of airflow in nasal cavity, Rhinology **46**(2), 137–143.

[20] Riazuddin, V.N., M. Zubair, I.L. Shuaib, M.Z. Abdullah, S.A. Hamid and K.A. Ahmad 2010: Numerical Study of Inspiratory and Expiratory Flow in a Human Nasal Cavity, Journal of Medical and Biological Engineering **31**(3), 201–206. doi:10.5405/jmbe.781.